SiO maser emission in Miras

M. D. Gray,[1][*] M. Wittkowski,[2] M. Scholz,[3,4] E. M. L. Humphreys,[5] K. Ohnaka[6] and D. Boboltz[7]

[1]*Jodrell Bank Centre for Astrophysics, Alan Turing Building, University of Manchester, Manchester M13 9PL*
[2]*ESO, Karl-Scwarzschild-Str. 2, 85748 Garching bei München, Germany*
[3]*Zentrum für Astronomie der Universität Heidelberg (ZAH), Institut für Theoretische Astrophysik, Albert Ueberle-Str. 2, 69120 Heidelberg, Germany*
[4]*Sydney Institute for Astronomy, School of Physics, University of Sydney, Sydney, NSW 2006, Australia*
[5]*Harvard–Smithsonian Center for Astrophysics, Cambridge, MA, USA*
[6]*Max-Planck-Institut für Radioastronomie, Auf dem Hügel 69, 53121 Bonn, Germany*
[7]*US Naval Observatory, 3450 Massachusetts Avenue, Washington, DC 20392-5420, USA*

ABSTRACT

We describe a combined dynamic atmosphere and maser propagation model of SiO maser emission in Mira variables. This model rectifies many of the defects of an earlier model of this type, particularly in relation to the infrared (IR) radiation field generated by dust and various wavelength-dependent, optically thick layers. Modelled masers form in rings with radii consistent with those found in very long baseline interferometry (VLBI) observations and with earlier models. This agreement requires the adoption of a radio photosphere of radius approximately twice that of the stellar photosphere, in agreement with observations. A radio photosphere of this size renders invisible certain maser sites with high amplification at low radii, and conceals high-velocity shocks, which are absent in radio continuum observations. The SiO masers are brightest at an optical phase of 0.1–0.25, which is consistent with observed phase lags. Dust can have both mild and profound effects on the maser emission. Maser rings, a shock and the optically thick layer in the SiO pumping band at 8.13 µm appear to be closely associated in three out of four phase samples.

Key words: masers – stars: AGB and post-AGB – circumstellar matter – stars: evolution – radio lines: stars.

1 INTRODUCTION

We present preliminary results from a significantly improved model of SiO maser emission from the circumstellar envelopes of Mira-type, and similar, long-period variable stars. The predecessor of this model, hereafter the 'old model', was used to compute synthetic spectra and images of SiO maser emission from a model star with parameters based on those of o Cet (Gray, Humphreys & Field 1995a; Humphreys et al. 1996). With additional phase information, the variation of the spectra and maps was computed over the stellar period of 332 d (Humphreys et al. 1997a; Gray & Humphreys 2000; Humphreys et al. 2002). The hydrodynamic solutions which provided the input physical conditions for the maser sites in the old model were taken from envelope computations by Bowen (1988), except in the earliest of these papers, Gray et al. (1995a), which used similar calculations by Willson (1987).

The old model used the (radial) density, velocity and gas kinetic temperature profiles from hydrodynamic solutions by Bowen

(1988) and Willson (1987). These hydrodynamic solutions also provided a radiative equilibrium temperature, T_{eq}, on the basis of geometrical dilution of the stellar continuum, and on the opacity of the gas, but no estimate of the abundance of SiO. The radius of the stellar photosphere was recalculated at each time-step, and defined as the radius where the optical depth equalled 2/3, but the effective temperature of the photospheric layer, whatever its radius, had a constant value, independent of the stellar phase. Dust was included in the pulsation model, and was dynamically significant at radii beyond the condensation zone (Bowen 1988). At radii where dust was present, the dust temperature was set equal to T_{eq}. The effect of dust was exerted through a spectrally averaged radiation pressure cross-section, a function of T_{eq} and the dust condensation temperature. The solutions did not specify a wavelength dependence for the dust opacity, or a dust number density, though this latter quantity could have been calculated, using sensible assumptions for the dust mass fraction, grain radius and mineral density (see Bowen 1988). Later Bowen models improved upon the version discussed above in several respects (Bowen 1990; Willson 2000), but these later models were never used by us for maser calculations.

[*]E-mail: mgray@aoc.nrao.edu

Report Documentation Page

1. REPORT DATE **2009**	2. REPORT TYPE	3. DATES COVERED **00-00-2009 to 00-00-2009**

4. TITLE AND SUBTITLE **SiO Maser Emission in Miras**	5a. CONTRACT NUMBER
	5b. GRANT NUMBER
	5c. PROGRAM ELEMENT NUMBER
6. AUTHOR(S)	5d. PROJECT NUMBER
	5e. TASK NUMBER
	5f. WORK UNIT NUMBER

7. PERFORMING ORGANIZATION NAME(S) AND ADDRESS(ES) **Centre for Astrophysics,Alan Turing Building,University of Manchester,Manchester M13 9PL,**	8. PERFORMING ORGANIZATION REPORT NUMBER

9. SPONSORING/MONITORING AGENCY NAME(S) AND ADDRESS(ES)	10. SPONSOR/MONITOR'S ACRONYM(S)
	11. SPONSOR/MONITOR'S REPORT NUMBER(S)

12. DISTRIBUTION/AVAILABILITY STATEMENT
Approved for public release; distribution unlimited

13. SUPPLEMENTARY NOTES

14. ABSTRACT

15. SUBJECT TERMS

16. SECURITY CLASSIFICATION OF:			17. LIMITATION OF ABSTRACT	18. NUMBER OF PAGES	19a. NAME OF RESPONSIBLE PERSON
a. REPORT **unclassified**	b. ABSTRACT **unclassified**	c. THIS PAGE **unclassified**	**Same as Report (SAR)**	**66**	

The old model made several simplifications and approximations, not inherent in the Willson and Bowen solutions, for constructing the infrared (IR) radiation field for maser pumping. The stellar component of IR radiation field assumed a fixed-radius stellar photosphere, and was modelled as a blackbody at the (constant) stellar temperature of 3002 K. Optically thin dust emission was crudely modelled as a blackbody at a single temperature, weighted by a power law in wavelength (Humphreys et al. 1996). As a consequence of these approximations, the radiative pump rate in any SiO ro-vibrational transition had no intrinsic variation with phase. Although the collisional part of the maser pump was modelled more accurately than the radiative part, a radiative component to the maser pumping was, however, always present (Humphreys et al. 1996, 2002). The old model used a constant value of 10^{-4} for the abundance of SiO, independent of both radius and phase, and, for the purposes of pumping calculations, hydrogen was assumed to be in molecular form, as no suitable set of rate coefficients was then available for the H + SiO system.

The stellar phase in the Bowen hydrodynamic solutions was defined as zero at the time a new shock left the stellar photosphere (Bowen 1988; Humphreys et al. 1996), and it was never possible reliably to relate this model phase to the optical, or near-IR, light curves of the star, despite several attempts to do so, for example Gray et al. (1998), Humphreys et al. (2002). It was therefore impossible to answer questions related to observed links between the light curves of SiO masers and the optical and near-IR continuum, for example Pardo et al. (2004). Polarization and the presence of minor isotopomers of SiO were also not included in the old model; these aspects of the problem remain absent in the new model, and will not be considered further in this paper.

Despite the drawbacks listed above, the old model was surprisingly successful when compared with observations. The single phase version (Gray et al. 1995a; Humphreys et al. 1996) predicted new masers with upper rotational states above $J = 6$. Such masers were subsequently detected in a number of stars, including examples from Miras and semiregular variables (Gray et al. 1995b; Humphreys et al. 1997b; Gray, Humphreys & Yates 1999). The ring structure of the SiO masers, found frequently in very long baseline interferometry (VLBI) observations (Diamond et al. 1994; Greenhill et al. 1995; Boboltz, Diamond & Kemball 1997), which indicates predominantly tangential amplification from a restricted range of radii, was also strongly supportive of the model. It is worth noting here that the model generated potential maser sites randomly throughout a sphere of significantly larger radius than the ring in which masers appear. If the model had been seriously inappropriate, it could have produced, for example, a smooth radial distribution, or, for predominantly radial amplification, a concentration of bright maser spots directly over the central star. The ring radius for the $v = 2, J = 1$–0 masers was found to be smaller, in a number of stars, than for $v = 1, J = 1$–0, in agreement with the model (Desmurs et al. 1999, 2000; Yi et al. 2000; Soria-Ruiz et al. 2004; Boboltz & Wittkowski 2005). The model prediction for the ring radius of the masers in the $v = 1, J = 2$–1 line at 86 GHz, is that it should have a comparable, or slightly larger radius than the ring formed by the $v = 1, J = 1$–0 masers, and be significantly less well populated. The second prediction seems to be in agreement with observations (Soria-Ruiz et al. 2004) but not the first. Observations of R Leo (Soria-Ruiz et al. 2007) confirm that, in this star at least, the $v = 1, J = 2$–1 transition forms in a ring further from the star than the $J = 1$–0 transition from the same vibrational state. Single-dish observations of a number of Miras with different dust temperatures (Nakashima & Deguchi 2007) showed a correlation of the flux in

the 8 μm continuum and the $J = 1$–0 masers from $v = 1$ and 2, which strongly suggests a radiative component to the maser pump.

The maser line ratios appear to be acceptable, given the uncertainties in what constitutes the background for unsaturated masers, except for the $v = 2, J = 2$–1 line which is much too strong when compared against observations. However, the weakness of this maser in real sources is very probably due to a line overlap with a water transition, for example Soria-Ruiz et al. (2004), and a molecular model of water was (and is) not included in our maser model.

When phase dependence is added, the old model remains broadly in agreement with interferometric observations, though with some discrepancies. For example, the model prediction of smaller maser rings, at $v = 2, J = 1$–0, compared with $v = 1, J = 1$–0, over the stellar cycle, is in agreement with observations (Cotton et al. 2004; Yi et al. 2005; Cotton et al. 2006; Wittkowski et al. 2007), as is the prediction of an rms amplitude variation of 5–10 per cent in the maser ring radius. These maser rings are also found to be inside the inner radius of the silicate dust shell, but Al_2O_3 dust may be colocated with the masers (Wittkowski et al. 2007). However, the predicted relation between SiO maser ring radius and SiO maser luminosity is not well reproduced, and varies both between different stars, and for different pulsation cycles of the same star (Cotton et al. 2004, 2006). Long-term monitoring of the $v = 1, J = 1$–0 line in the Mira TX Cam (Diamond & Kemball 2003) shows motions dominated by shock-driven outflow for part of the stellar period, whilst the remainder is dominated by infall under gravity. This behaviour agrees with the model assuming a reasonable link between the model and optical phases, though the variation in the maser ring radius is somewhat larger (18 per cent) in TX Cam. It should also be noted that TX Cam exhibits considerable asymmetric behaviour, and some maser features move outwards, for example, even during the infall-dominated phase. If the model to optical phase relation used by Yi et al. (2005) is adopted (model phase = 0.78 at optical maximum) then the disrupted, weak maser ring structure found near optical minimum in TX Cam is also consistent with observations, though any linking of the old model and optical phases should be treated with great caution for reasons discussed above.

Single-dish monitoring observations suggest that shock waves, at least of a type which take a significant fraction of the period to cross the gap between the stellar photosphere and the maser zone, cannot be responsible for the maser pumping, though some observations still suggest a coupling between the pump and the kinematics of the envelope gas. See Cotton et al. (2006) for a detailed discussion of the problems involved in relating results from interferometric and single-dish observations. Whilst it is not true to say that the old model is entirely collisionally pumped, a major drawback is that it cannot explain correlation between the light curves of SiO masers and radiation in the IR pumping bands. It is clear that such correlations exist: Pardo et al. (2004) found that the optical, near-IR continuum and SiO masers share the same period in a sample of 13 Mira variables. They also found the IR and SiO maser peak luminosities coincided to within 0.05 of a stellar period. The IR data in Pardo et al. (2004) is at 4.9 and 3.5 μm, and therefore does not include the crucial $\Delta v = 1$ pumping band of SiO at 8 μm. McIntosh (2006a) finds that the maxima in the 43-GHz masers from $v = 0, 1, 2$ occur simultaneously to within 0.066 periods in o Cet. As the $v = 0$ maser ring was apparently much larger than those at $v = 1$ and 2, this suggests that the pumping is predominantly radiative. However, the old model makes no prediction about $v = 0$ masers, and the difference between the ring radii at $v = 1$ and 2

is sufficiently small (∼0.1 to ∼0.2 au, dependent on phase) that a shock of reasonable speed could propagate between them in 0.066 of a period (22 d). These observations (McIntosh 2006a) also did not detect any disruption of the maser activity, due to shock arrival, near optical minimum. Further analysis with the same dataset from o Cet (McIntosh 2006b) finds that SiO maser flux density in the $v = 1$, $J = 1–0$ transition is correlated with the velocity centroid of the emission. McIntosh (2006b) offers two possibilities for this correlation: either the pump affects the kinematics of the maser region (i.e. shocks strongly influence maser amplification, principally through disruption of velocity-coherent gain paths, but also by heating and compressing the gas) or that the maser pump and (independent?) kinematic effects combine to produce the observed maser spectra. The current authors find this second possibility hard to reconcile with the model, since in the large velocity gradient (LVG) approximation used, the Sobolev optical depth in any direction is dependent upon the velocity gradient, and therefore the kinematics are intimately coupled to the pumping scheme. Similar observations for the Mira R Cas (McIntosh & Haynes 2007) largely agree with those from o Cet. However, it is interesting that for one maximum, the peaks of the $v = 1$ and 2, $J = 1–0$ masers are significantly separated in phase.

The pulsating atmospheres of Miras are very extended because of dynamic events, such as shocks. These extended atmospheres exhibit phase-dependent temperature and density stratifications, optically thick molecular layers, and dust formation; see for example Scholz (2003). Observed radii of Miras have been found to depend on both phase and wavelength of observation, which is consistent with the predictions of dynamic models, in which molecular layers lie above the continuum-forming layer (Thompson, Creech-Eakman & van Belle 2002; Ohnaka 2004; Perrin et al. 2004; Ohnaka, Scholz & Wood 2006b; Wittkowski et al. 2008). In a series of experiments (Boboltz & Wittkowski 2005; Wittkowski et al. 2007) mid-IR interferometric measurements made with the VLTI were made near contemporaneously with VLBA observations of the 43-GHz masers in $v = 1$ and 2 towards the Mira S Ori. Models (Ireland et al. 2004a,b) were fitted to four observing epochs, with an estimated error of ≲0.15 pulsation periods between the model and optical phases. Both the IR photosphere radius, defined as the radius at 1.04 μm, and the radius of the optically thick layer near 8 μm (the $\Delta v = 1$ SiO pumping band) vary in phase with the optical light curve, as far as can be judged from the limited phase sampling. Importantly, the radius of the 43-GHz maser shells is slightly larger than this 8-μm quasi-photospheric band radius at all four observing epochs. If this optically thick layer represents high-density post-shock gas, then the position of the shock would be tightly correlated with the light curve at this frequency, very possibly leading to a resolution of the radiative/collisional pumping debate. Recent work by Woodruff et al. (2008) suggests that, with certain caveats, the conclusions obtained for S Ori can be extended to a sample of other Mira variables.

2 IMPROVEMENTS TO THE MODEL

Our improved model removes many of the defects inherent in the old version because of its restricted information about conditions in the circumstellar envelope. In particular, the new version includes radii for several optically thick layers, for both continua and restricted-wavelength bands, as a function of phase. The set of bands includes all the IR pumping bands of SiO which are accessible to the model. Other features of the new model include an accurate estimate of the IR radiation field from dust, sufficient chemistry to provide abundances for SiO and its main collision partners, and new

rate coefficients for collisions of SiO with hydrogen atoms. A link between the model phase (in terms of the shock position) and the stellar light curve is implicitly included in the model data.

At this point we digress to make some definitions regarding the optically thick layers introduced above. We reserve the word 'photosphere' to mean a continuum-forming layer, and we always use this word with a modifier which specifies the region of the spectrum to which it applies. In particular, we define 'IR photosphere' to be the continuum-forming layer at 1.04 μm where the optical depth is equal to 1. This wavelength was chosen because it is in a region little contaminated by molecular line absorption. We use 'radio photosphere' to be the continuum-forming layer in the radio region. This is less well defined, but, in the context of SiO, can be taken to mean the region of the electromagnetic spectrum occupied by the pure rotational lines of SiO in general, and the maser lines at 43 and 86 GHz in particular. When referring to other work, for example the hydrodynamic solutions of the old model, which does not match the precise definition of the IR photosphere, we use the expression, 'stellar photosphere', to describe the continuum-forming layer in the optical and near-IR. Where photospheric radii have already been mentioned in Section 1, they conform to the above definitions.

Each SiO pumping band has a quasi-photospheric, optically thick, layer, due to the presence of large numbers of molecular lines, mostly from water. These layers have radii computed as $\tau_\lambda = 1$ radii based on the definition of the filter radius in Scholz & Takeda (1987) using a box filter of width 0.1 μm. When referring to these optically thick layers, the form of words we adopt is 'optically thick band radius', or 'optically thick layer'. When referring only to the radii of such layers, we write a shorter form, specifying the wavelength of the band in microns, followed by 'radius'. For example, to refer to the radius of the optically thick molecular layer in the $\Delta v = 1$ band of SiO, we use the shorthand '8.14 μm radius'.

2.1 Hydrodynamic solutions

The hydrodynamic solutions used in this paper are based on those published in Ireland et al. (2004a) and Ireland et al. (2004b). We are particularly interested in the M-series of models, drawn from the latter work. All these models have a pulsation period of 332 d, like the real star o Cet and the old model. However, other parameters of the M-series models might be more appropriate for a model of R Leo. The abundance of SiO is computed by an additional code by Ohnaka. This code employs equilibrium chemistry, including 34 elements and 235 molecular species, and assumes solar abundances of the reactants. Optically thick band radii are provided in the SiO ro-vibrational pumping bands at 2.03, 2.74, 4.09 and 8.14 μm, corresponding to vibrational changes, respectively, of $\Delta v = 4, 3, 2$ and 1.

The M-series of models is described in detail in Ireland et al. (2004b). The important stellar parameters are briefly listed here in Table 1. The radius and effective temperature refer to a non-pulsating 'parent' star, where these values are independent of phase. The parent parameters are based on a layer where the Rosseland mean optical depth is 1. There are 20 M-series models altogether, some with the subscript n, denoting a new model, first published in Ireland et al. (2004b). Other models appeared previously in either Hofmann, Scholz & Wood (1998) or Tej et al. (2003). Each model has a cycle (pulsation) number and a phase within that cycle. At present the samples range from phase 0.49 of cycle 0 to phase 0.50 of cycle 2, giving ten models per cycle, though these are not evenly spaced in phase. Model parameters are listed in table 1 of

Table 1. Parameters for the M-series models (Ireland et al. 2004b). The radius R_p refers to the parent star (see text). The effective temperature and luminosity are computed for the non-pulsating parent star.

Parameter	Symbol	Value
Period	P	332 d
Mass	$M/M_\odot$	1.2
Metallicity	$z/z_\odot$	1.0
Luminosity	$L/L_\odot$	3470
Radius	$R_p/R_\odot$	260
Temperature	T_{eff}	2750 K

Figure 1. Radial velocity of model M21n as a function of radius, showing the presence of outward-moving shocks. The shape of the outer shock appears smoothed in the model for computational reasons (dashed line: without smoothing applied).

Figure 2. Kinetic temperature of the gas in model M21n: the constant temperature of 741 K at large radii is artificially set, since the equation of state is poorly known at the very low temperatures of the uppermost layers.

Figure 3. Number densities of H_2 (solid line), He (dashed line), H atoms (chained line) and SiO (complex line).

Ireland et al. (2004b). Phase values are given in terms of the optical light curve and are estimated accurate to about 0.1 pulsation periods absolutely, but more accurately relatively (0.01–0.02 periods). An estimate of the phase-variable IR photospheric radius is given as $R_{1.04}$ for each model. The basic models are dust-free, and extend radially to $5R_p$, where R_p is the radius of the parent star. This is a considerably smaller radial coverage than in Bowen (1988), but this has no consequences if the water and OH maser zones are ignored. We also note that the models we use are developed from grey dynamic models which extend to considerably larger radii than $5R_p$, and which establish the initial pressure stratification for the refined non-grey models.

In this paper, we use the same models which were used in the fit to S Ori (Wittkowski et al. 2007). These are M21n, M22, M23n and M24n, which have respective optical phases of 0.10, 0.25, 0.30 and 0.4. The stellar parameters of S Ori differ from those used for the M-series of models in pulsation period, radius and mass. The M-models were used as the best available option to describe the dynamic atmosphere of S Ori, scaling the period to phases between 0 and 1, and the radius to match the observed angular diameter of S Ori. See also the discussion in Wittkowski et al. (2007). We do not expect these scaling operations to lead to strong effects, but it should be kept in mind that remaining differences between model predictions and observations of S Ori might arise from this moderate mismatch of stellar parameters.

As examples of the behaviour of the physical conditions in the model atmosphere we plot, for M21n, the radial velocity (positive means outflow), kinetic temperature, and the number densities of SiO and its main collision partners as functions of radius in Figs 1–3, respectively. A strong inner, and a weaker outer, shock are visible in Fig. 1 at radii of 1.57 and 3.00 R_p (2.84 × 10^{13} and 5.43 × 10^{13} cm). The shock fronts are slightly smeared out in the models (see Ireland et al. 2004b) and affect both the temperature and density graphs. The shape of the SiO number density curve follows closely that of H_2. The optically thick band radii in the SiO pumping bands at 2.03, 2.71, 4.06 and 8.13 µm are, respectively (2.51, 4.18, 2.13 and 3.98)×10^{13} cm, so the 8.13-µm layer, at this phase, actually lies outside the radius of the strong, inner shock.

2.2 Dust and the IR radiation field

In Wittkowski et al. (2007), the dust-free hydrodynamic solutions described above were complemented by ad hoc radiative transfer models of the dust shell, using the radiative transfer code MCSIM_MPI by Ohnaka et al. (2006a). A dust-free model of the M-series was combined with a dust shell model using dust shell parameters so that the overall models fitted the four epochs of observations of S Ori.
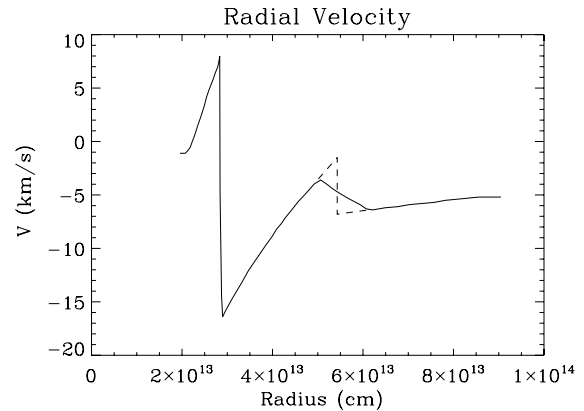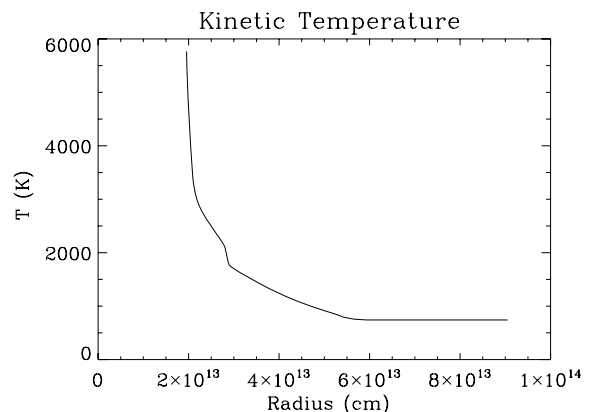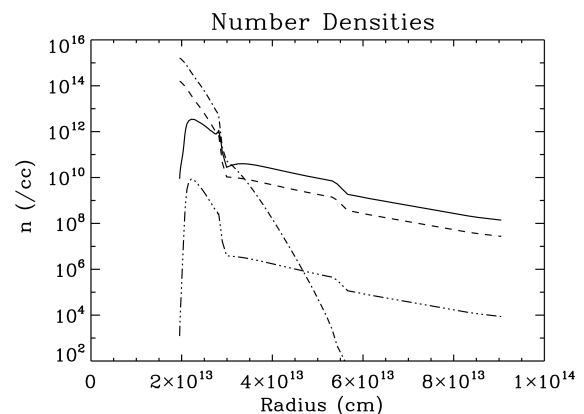
The best-fitting overall models for the four epochs of observation, A, B, C, D, have parameters listed in Table 2. We therefore adopt as standard, the pairings epoch A + M22, epoch B + M24n, epoch C + M23n and epoch D + M21n, and use these in the work that follows, except in Sections 4.3 and 5.2.

Table 2. Standard pairings of dust epochs and hydrodynamic solutions with parameters of the model star and dust shells. Observational phases (ϕ_{obs}, Column 2) refer to S Ori (Wittkowski et al. 2007). Theoretical phases (ϕ, Column 4) are the phases of the hydrodynamic model, on the optical scale, fitted to each epoch. Column 5 is the ratio of the inner radius of the dust shell to the IR photospheric radius, and Column 6 is the visual optical depth of the dust shell.

Epoch	ϕ_{obs}	Model	ϕ	$R_{in}/R_{1.04}$	τ_V
A	0.42	M22	0.25	1.8	2.5
B	0.55	M24n	0.40	2.0	2.5
C	1.16	M23n	0.30	2.2	1.5
D	1.27	M21n	0.10	2.4	1.5

In the modelling of S Ori, combinations of Al_2O_3 and silicate dust were tested, but better fits were obtained from dust-shell models without silicates. Therefore, epochs A–D dust shells use Al_2O_3 dust only, which is assumed to be in the form of spherical grains of a single radius, $a = 0.1\,\mu m$. Each dust epoch provides, as a function of radius, the number density and temperature of the dust. Optical efficiencies for absorption and scattering were taken from Koike et al. (1995) for wavelengths shortward of $7.8\,\mu m$, and from Begemann et al. (1997) for longer wavelengths. These optical efficiencies, the table of number densities and temperatures, together with stellar parameters provide all the information necessary to compute the angle-averaged intensity of the IR dust radiation field in the circumstellar envelope (see Section 4).

Silicate dust can optionally be included in the dust shell calculations. When it is so included, the optical efficiencies are the 'warm silicate' variety from Ossenkopf, Henning & Mathis (1992). The silicate grains are assumed to be spheres with the same single radius as their Al_2O_3 counterparts. Dust of this type has been used in a model of the envelope of the Mira GX Mon (Boboltz D. et al., in preparation). We note that the dust shell extends to substantially larger radii ($R_{in} \sim 2\,R_p$ and $R_{out}/R_{in} = 1000$) and, when present, the silicate dust is found at larger radii (inner radius $\sim 4\,R_p$) than the Al_2O_3 dust.

We plot, in Fig. 4, the number density of Al_2O_3 dust as a function of radii for the four epochs A–D. Fig. 5 shows the dust temperature as a function of radius for the same four models.
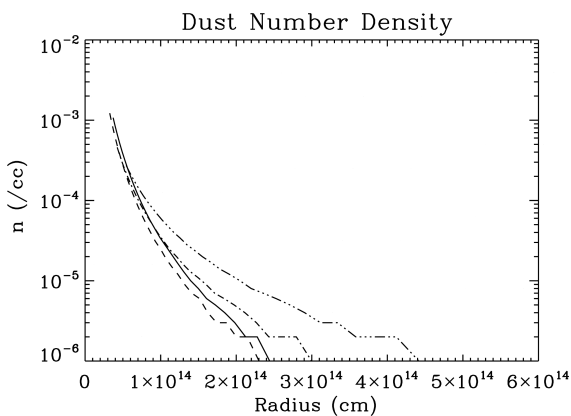

Figure 4. Number density of Al_2O_3 dust as a function of radius for the four epochs A (solid line), B (dashed line), C (chained line) and D (complex line).
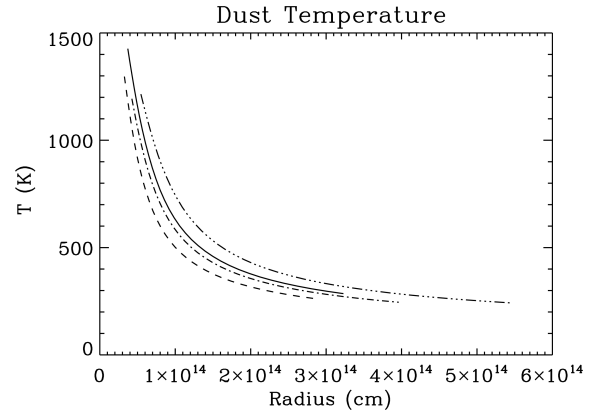
Figure 5. As for Fig. 4, but showing the dust temperature. Epoch B has the smallest inner radius, followed by epoch A. Epoch A has the highest temperature at its inner radius.

As noted in Section 1, dust was dynamically important in the hydrodynamic solutions of the old model, but not so with the dust shells attached to the dust-free hydrodynamic solutions of the current model. In this connexion, we note that studies by Ireland & Scholz (2006) found that dust did not noticeably affect the density and temperature stratification of the model for radii $\lesssim 2\,R_p$ in Miras with parameters similar to o Cet or R Leo. Preliminary results from very recent calculations (Ireland, Scholz & Wood 2008), which do include the formation and dynamical effects of dust, suggest that this view is correct, though only a small subset of the full phase and cycle data is currently available. These conclusions from models are supported by measurements of the inner dust radius with MIDI (Wittkowski et al. 2007), which place it in range 1.8–2.2 IR photospheric radii.

2.3 Rate coefficients for H + SiO

For details of the rate coefficients used for collisions between H_2 and SiO, see Humphreys et al. (1996) and references therein. These rate coefficients were originally computed for He + SiO collisions, and can easily be reset to the latter system by changing the total and reduced masses.

The inner regions of the circumstellar envelope contain substantial amounts of hydrogen in atomic form (see Fig. 3). We have therefore included a set of rate coefficients for H + SiO collisions. For details of the computations of the potential surface and collision cross-sections, see Jimeno, Gray & Balint-Kurti (1999) and Palov et al. (2002); for calculation of the rate coefficients from these cross-sections see Palov et al. (2006). Rate coefficients can be computed for any ro-vibrational transition in the first six vibrational states ($v = 0$–5) for rotational states from $J = 0$–40, and with a maximum change in rotational quantum number of $|\Delta J| = 40$. The accuracy of the rate coefficients degrades progressively above 5500 K, but this is not a problem with the hydrodynamic solutions used in this paper, where the maximum kinetic temperature is ~ 6000 K (see Fig. 2). The H + SiO rate coefficients are different, and systematically larger than for the He + SiO system. They are of similar magnitude for $\Delta v = 0$ transitions, but larger by a factor of 10–100 for the vibrationally inelastic case. The expected decay in the magnitude of rate coefficients as Δv increases is also rather slow, so that H + SiO

collisions can efficiently make rather large changes in vibrational state.

3 REMAINING PROBLEMS

The improvements discussed in Section 2 do not solve all the problems with the model, and actually introduce one or two new, though minor, difficulties. Most of these relate to our lack of knowledge of the position of the radio photosphere. In addition, we still rely on the LVG approximation for the maser pumping code, and we have no rate coefficients which are based on the true $H_2 + SiO$ collisional system, though some new calculations may soon become available (Bienieck 2008).

3.1 The radio photosphere

The new hydrodynamic solutions (Section 2.1) provide phase-dependent radii for the optically thick molecular layers in the four ro-vibrational pumping bands which are possible in our model, which has 200 levels distributed equally between the first five vibrational states ($v = 0$–4). However, the pure rotational transitions cannot be assigned to any of these bands, and the position of the optically thick layer, or radio photosphere, at the longer wavelengths (submillimetre to cm) of these rotational lines is much less certain. The radiation field from the dust can be ignored for the pure rotational lines because of the very low optical efficiencies at these wavelengths, but see Section 3.2 below. Therefore, we need to consider only the stellar radiation from the point of view of pure rotational radiative maser pumping.

Estimates of the radius of the radio photosphere have been made by Reid & Menten (1997), using three frequencies, all lower than any SiO pure rotational lines. The opacity for the radio photosphere is maintained by free–free interactions of electrons with neutral H and H_2, the electrons originating from ionization of K and Na. Fig. 10 of Reid & Menten (1997) strongly suggests that the radius of the radio photosphere at the SiO frequencies (in the approximate range 40–1500 GHz) is smaller than at the measured frequencies, and may change by a factor of $\sim$1.3 over this range of frequencies. Overall, Reid & Menten (1997) give a figure of $2R_*$ for the radius of the radio photosphere, where R_* is the radius of the stellar photosphere. The figure of $2R_*$ still appears in more recent work (Reid & Menten 2007), but the radio photosphere is also linked to the optically thick molecular layer which becomes opaque in the mid-IR. With this limited information, it is difficult to make a good choice for the radius of the radio photosphere, but we have chosen to associate it with the molecular layer, as in Reid & Menten (2007), and we have set the radius of the radio photosphere equal to the optically thick band radius at the longest IR waveband (the 8 μm radius). This means that the radio photosphere, like the optically thick layers in the IR bands, moves with the stellar pulsations. We also note that if we can set $R_* \sim R_p$, then this choice of radius in the radio region is in good agreement with the figure of $2R_*$. However, given the uncertainties in the position of the radio photosphere, and the fact that the maser lines cover an order of magnitude in wavelength, so there is unlikely to be one optically thick radius for all these lines, we allow the choice of maser sites to vary from the smallest radius in the hydrodynamic solution, at each phase, up to the constant value of $5R_p$. We can then investigate the effect of making the radius of the radio photosphere very small, and subject the site distribution to later exclusions on the basis of the larger 8 μm radius discussed above.

3.2 Maser backgrounds

In the old model, the background amplified by the masers was set to a Planck function at the gas kinetic temperature local to each maser site, without much justification for this choice. However, given that the allowed masers in the model are a subset of the pure rotational transitions discussed above in Section 3.1 (those with upper $J \leq 10$), the presence of a radio photosphere at radii similar to those of the maser zone makes this choice rather more acceptable, and we keep it for the new model. The alternative would be to integrate along the line of sight through the dust shell over all the dust and SiO spontaneous emission lying behind the maser site. However, this background is optically very thin, and would produce a far weaker background than optically thick emission from the radio photosphere. Of course, for saturating masers, it does not matter what the background radiation is. However, the amplifying column required to reach saturation is significantly longer for a weak background, so that a background originating from the radio photosphere would, on average, lead to a brighter set of masers.

An interesting possibility is that it is the background which breaks the symmetry of the maser shells in real stars, leading to the distribution of spots that we see, instead of an unbroken ring. In the old model, we appealed to variations in the SiO abundance to break the symmetry, but as we now have this as a smooth function of radius (see Fig. 3) it is less acceptable to do this. A purely speculative idea at present is that the maser sites lie above regions which are like extensions to the radio photosphere, with enhanced electron abundance from above average ionization of the alkali metals, and consequently high input backgrounds to overlying masers. These sites would then have the advantage over surrounding regions of needing shorter amplifying columns to reach the same maser intensity. Asymmetries of this type in the molecular layer, which forms the optically thick band radius at 8 μm have already been found (Weigelt et al. 1996; Ragland et al. 2008), although it is not clear that these would extend, in wavelength, to the radio region. The choice of maser sites in our computations remains one of random selection (Humphreys et al. 1996).

3.3 Point-like masers

The use of the LVG approximation for the transport of the pumping radiation simplifies the radiation transfer problem, but there is a considerable price to pay for this simplicity. The approximation is essentially local, so that a region constituting the maser is effectively defined by the distance (which can vary with direction) required for the radiation line shape to be shifted out of resonance with the response line shape of the molecules. When we pick the coordinates of a maser site, there is still an assumption that the physical conditions within this, velocity bounded, LVG zone are equal to those at the selected coordinates.

3.4 LTE chemistry

The abundances of the atomic and molecular species used in the current model are based on local thermodynamic equilibrium (LTE) chemistry. This amounts to an assumption that the network of chemical reactions comes to equilibrium on a time-scale which is short compared with important hydrodynamic time-scales in the envelope. It is likely that non-LTE chemistry is important is establishing the time-varying populations of a number of species, including CO, HCN, CS and SiO, as predicted in models by Cherchneff (2006). Detection of all these molecules in a sample of asymptotic giant

branch (AGB) stars of widely varying C/O abundance strongly supports the model predictions (Decin et al. 2008). There is a brief discussion of non-LTE effects pertaining to models of the type used in this paper in Ireland et al. (2008).

4 COMPUTATIONS

4.1 IR pumping radiation

We briefly consider the conversion of the dust optical efficiencies described in Section 2.2 to the inputs required by the maser model: namely effective grain areas and angle-averaged intensities ($\bar{J}$) at the wavelength of every electric-dipole-allowed transition in the SiO model. The areas were trivially obtained from the optical efficiencies, since the grains are modelled as having a unique radius.

To compute the angle-averaged intensities, we solve, for each tabulated dust wavelength and radius in the dust model, the radiative transfer equation,

$$\frac{dI}{d\tau} + I = \frac{B(T_A)}{1 + (\kappa_S/\kappa_A) + (\sigma/\kappa_A)} + \frac{B(T_S)}{1 + (\kappa_A/\kappa_S) + (\sigma/\kappa_S)} + \frac{\bar{J}}{1 + \kappa/\sigma}, \quad (1)$$

which is written for the most complicated situation considered, with a two-component dust shell of Al_2O_3 (subscript A) and silicate (subscript S). Absorption coefficients (κ) and scattering coefficients (σ) are written without a subscript when summing over both dust types, for example $\sigma = \sigma_A + \sigma_S$. The optical depth is given by the standard expression, $d\tau = (\kappa + \sigma) ds$, where ds is the element of distance along a ray. With the single-radius dust approximation, it is possible to write the ratios that appear in equation (1) directly in terms of the optical efficiencies for absorption, Q_{abs}, and scattering, Q_{sca}, for example

$$\frac{\kappa_S}{\kappa_A} = \frac{n_S Q_{abs,S}}{n_A Q_{abs,A}}, \quad (2)$$

where n_S (n_A) is the number density of silicate (Al_2O_3) dust. Similar expressions can be used for the other ratios. The thermal emission terms contain Planck functions, $B(T)$, for the appropriate dust temperature, and the scattering term contains the angle-averaged intensity, $\bar{J}$, defined in the spherical geometry used here as

$$\bar{J} = \frac{1}{2} \int_{-1}^{1} I(\mu) \, d\mu. \quad (3)$$

We note that as equation (1) contains $\bar{J}$, the solution is iterative, with specific intensities for each value of $\mu = \cos\theta$ being computed with the most recent estimate of $\bar{J}$, before a new value is found from equation (3). The boundary conditions used in the solution of equation (1) were to use a Planck function at the kinetic temperature of the appropriate SiO band radius for values of μ that intersected such an optically thick layer. For other values of μ, a Planck function at the cosmic microwave background (CMB) temperature was used. A value of $\bar{J}$ was calculated for each radius in the hydrodynamic solution, and for each dust wavelength.

We next calculate the dust contribution to the pumping rates in each SiO transition. For a transition with upper level, u, and lower level, l, the dust contributions are $B_{ul}\bar{J}$ and $B_{lu}\bar{J}$, where B_{ul} and B_{lu} are the Einstein B coefficients for the transition. We first assign each transition to either one of the IR pumping bands, or as 'radio', a blanket designation for all the pure rotational lines. The input data for the dust routine is then read in: the dust areas tabulated by wavelength, the dust temperatures and number densities tabulated
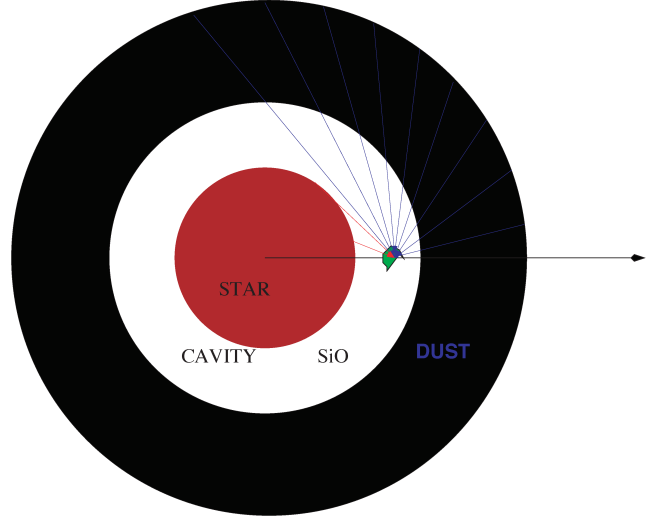

Figure 6. A maser site shown in the cavity between an optically thick layer, marked as the star, and the surrounding dust shell [case (ii) in the text]. Rays at various possible angles are shown converging on the maser site, where they are angle averaged. The size of the optically thick layer is different, in general, for each SiO pumping band and pulsational phase.

by radius, and the dust mean intensities, computed as discussed above, tabulated by both radius and wavelength. These mean intensities are required for calculating the scattering contribution to the dust radiation field. Then, considering the radius of a single maser site, a geometrical dilution factor is calculated relative to the optically thick band radius at each pumping band. In a loop over the SiO spectral lines, we then classify the maser site as in one of three basic positions for the current line. Case (i) is that the site is inside the band radius, in which case the pump in the current line corresponds to a blackbody at the temperature of the site radius and wavelength of the line; there is no dust contribution. Case (ii) is that the maser site is in a dust-free gap between the band radius and the dust shell, for example Fig. 6. The final possibility, case (iii), is that the maser site is inside the dust shell. In both case (ii) and case (iii), a radiative transfer equation is solved for the current transition. Rays were traced at a number of angles through the envelope, with each ray terminating on the maser site. Values of the dust areas, and mean intensities at the line wavelength were obtained from spline interpolations from the input tables for each site radius. A given ray had two possible starting conditions: an optically thick layer, yielding a blackbody at the temperature of that layer, or an interstellar value, taken to be the CMB. Case (iii) required the stellar contribution to undergo some extinction due to the dust. Angle-averaging of the rays produced the required mean intensity at the wavelength of a particular line, and this was trivially converted to a pump rate.

4.2 Size of radio photosphere

We have noted in Section 3.1 that there is a considerable uncertainty in the size of the radio photosphere for the maser lines. We here show the difference between a model based on the standard value, which is equal to the 8 μm radius, and an otherwise identical model in which the radio photosphere has been taken to coincide with the IR photosphere. In both cases we use Model 1 (see Table 3), and the same distribution of maser spots. In the first version of the model (1a) we allow masers with nominal positions outside an IR photospheric radius of $1.21 R_p$ (the 1.04 μm value) to grow;

Table 3. Job runs to investigate the effect of variation of the dust shell only. All other parameters are for the model with structure M21n (Ireland et al. 2004b).

Job number	Structure	Dust epoch
1	M21n	D
2	M21n	C
3	M21n	B
4	M21n	A

in Model 1b, we exclude masers inside $2.20\,R_{\rm p}$, corresponding to the $8\,\mu$m radius. This exclusion is based on the idea that, though SiO molecules may exist at the site, and these may be successfully pumped, optically thick layers at larger radii, and at the maser frequency, will prevent external observers from seeing the emission.

4.3 Variation of dust envelopes

Initially, we considered a single hydrodynamic solution, M21n, and ran the maser code for 1500 maser sites, as in the old model, for each dust epoch in turn. We note that M21n is actually paired with dust epoch D, but we ran it with the other three epochs simply to look for the effects of varying the dust component of the radiative pump. The models testing the variation of the dust envelope are listed in Table 3. The seed for the random number generator was the same for all these models. As they also have the same structure, which means the same parent radius for the star, the maser positions were the same for all the models. Results for the dust variation models appear in Section 5.2.

4.4 Phase samples

In this set of computations we ran jobs for four hydrodynamic solutions, each with its standard dust epoch. Details of these jobs appear in Table 4. Note that job 1 appears in both the dust variation and phase sample data. The models all used 1500 maser sites, randomly distributed between the (phase dependent) IR photospheric radius (see Table 4) and an outer radius of $5\,R_{\rm p}$. In view of the small number of phase samples, we did not attempt to advance the model with phase, the method adopted in Humphreys et al. (2002), but instead we rerandomized the maser positions for each new model. Results appear in Section 5.3.

Table 4. Job runs to investigate the effect of stellar phase on the intensity and distribution of maser spots. Structure designations are from Ireland et al. (2004b). Phases are based on the optical light curve. Stellar radii (Column 5) are based on the IR photosphere, at $1.04\,\mu$m, and given in units of the 'parent' radius of the star, where $R_{\rm p} = 1.809 \times 10^{13}$ cm. $8.13\,\mu$m radii, assumed equal to the size of the radio photosphere, are also in parent units.

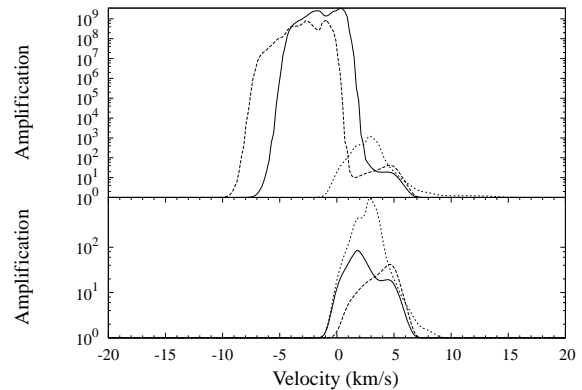| Job	Structure	Dust	Phase	$R_{1.04}/R_{\rm p}$	$R_{8.13}/R_{\rm p}$
1	M21n	D	0.10	1.21	2.20
5	M22	A	0.25	1.10	1.77
6	M23n	C	0.30	1.03	1.73
7	M24n	B	0.40	0.87	1.69

Figure 7. Spectra of the three SiO maser lines $v = 1, J = 1$–0 (solid line), $v = 1, J = 2$–1 (dashed line) and $v = 2, J = 1$–0 (dotted line) for Model 1a (top) and Model 1b (bottom). These models differ only in the assumed size of the radio photosphere, which is smaller in Model 1a (upper graphs).

5 RESULTS

5.1 Size of radio photosphere

In Fig. 7, we show spectra from Model 1a (top) and Model 1b (bottom). Recall that in Model 1a, the radio photosphere is small, coinciding with the IR photosphere, which at this phase has a radius of $1.21\,R_{\rm p}$. By contrast, in Model 1b, the radio photosphere coincides with the $8.13\,\mu$m radius, equal to $2.20\,R_{\rm p}$. The three spectra shown in each panel are the three most commonly observed lines: $v = 1$, $J = 1$–0 and $J = 2$–1 and $v = 2, J = 1$–0. In both lines from $v = 1$, Model 1a (top panel) produces extremely high amplification masers. These are emitted by a population of maser sites, just outside the small radio photosphere of this model. We refer to this population as the 'bright, inner objects' to distinguish them from more modest maser emitting sites at larger radii in the envelope.

The $v = 2$ transition has the same shape in both panels, so the bright, inner, objects do not emit significantly in this line. Emission from the bright inner masers in both the $v = 1$ transitions can be seen to be blueshifted by ~ 5 km s^{-1} relative to the emission from the outer population. This shift arises naturally if the inner population of masers is associated with post-shock gas inside the inner shock (see Fig. 1)

In Fig. 8 we show synthetic maps of the 43 GHz $v = 1, J = 1$–0 masers, the most commonly mapped transition with VLBI instruments. In the upper figure, we again have the smaller radio photosphere, allowing the appearance of an inner ring of very bright masers, with a projected radius close to $\sim 1\,R_{\rm p}$. The lower panel shows the maser distribution with the larger radio photospheric radius of $2.20\,R_{\rm p}$. The maser ring in the lower panel has properties which are similar to those of a 'quiet' phase in the old model, and a radius which is in good agreement with observations. If the spots of the inner ring had similar dimensions and beam angles to those at larger radii, they would be a factor of 10^6 times brighter than those found in the old model, or at larger radii in the current model. As masers of this power are not observed, we conclude that such a small radio photosphere is not realistic, and we adopt the larger, standard, value from here on. We note that, even if we adopt the smaller radius for the radio photosphere, the masers still form in two distinct rings: there is not a population of maser spots of similar brightness extending from the outer ring inwards towards the inner group, though the mapping software used to generate Fig. 8 suggests that there may be. In fact, if we adopt a radio photospheric radius of
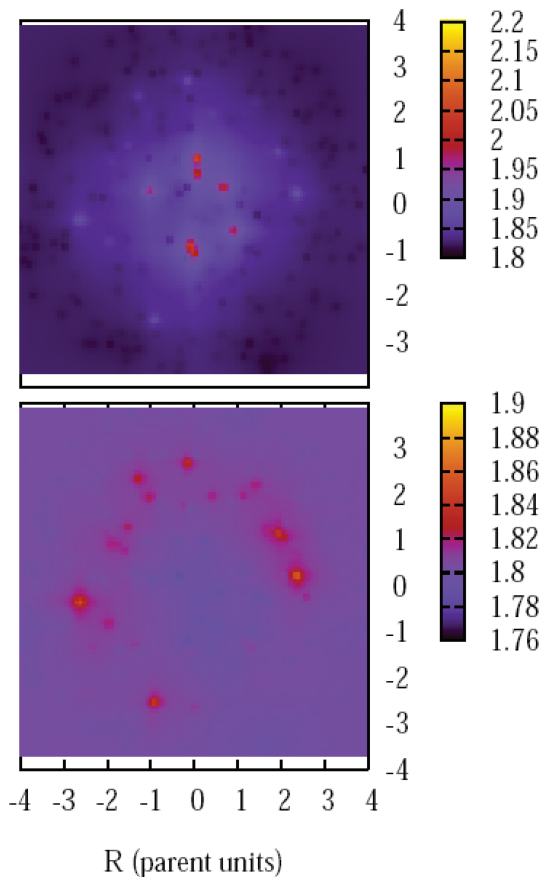
Figure 8. Modelled maps of the $v = 1, J = 1$–0 transition with radio photospheric radii of 1.21 R_p (top) and 2.20 R_p (bottom). In the top panel, the log to the base 10 of the maser amplification is clipped at a value of 3, for any individual spot, to render the outer ring visible.

Figure 9. Model spectra for the maser transitions $v = 1, J = 1$–0 (top panel), $v = 1, J = 2$–1 (middle) and $v = 2, J = 1$–0 (bottom panel). Each panel has four versions of the spectrum corresponding to: Model 1, dust epoch D (solid line), Model 2, dust epoch C (long-dashed line), Model 3, dust epoch B (short-dashed line) and Model 4, dust epoch A (dotted line). The hydrodynamic solution is M21n in all cases.

1.39 R_p, corresponding to the 2.03-µm pumping band, the spectra and maps are almost identical to Model 1b, which features only the outer ring. This intermediate radius is already large enough to exclude all the very bright spots with no observational counterparts.

An interesting feature of the outer ring (Fig. 8) is a 'missing' sector in the (observational) south-west. This arises purely from random selection of sites, but such gaps do sometimes appear in the maser rings of real stars.

We adopt the larger radio photosphere from now on, corresponding to the 8.13-µm pumping band. Therefore, the extremely bright, inner ring of masers is excluded. However, the fact that this inner ring can be produced raises an interesting point about the origin of the maser sites. If we assume that the motion of a typical maser spot is outward, more than inward, then we expect new spots to feed into the distribution near its inner edge, and therefore close to the radio photosphere. How do these new spots appear, and do they predominantly 'switch on' at a particular phase? The old model did not address this question because it set an initial random distribution of spots at model phase zero (when a new shock left the stellar photosphere) and subsequently adjusted the positions of these spots with phase, following the velocity field in the envelope. There was no source of new spots. The new model may be able to derive a phase for the appearance of a new ring once more phase samples are available.
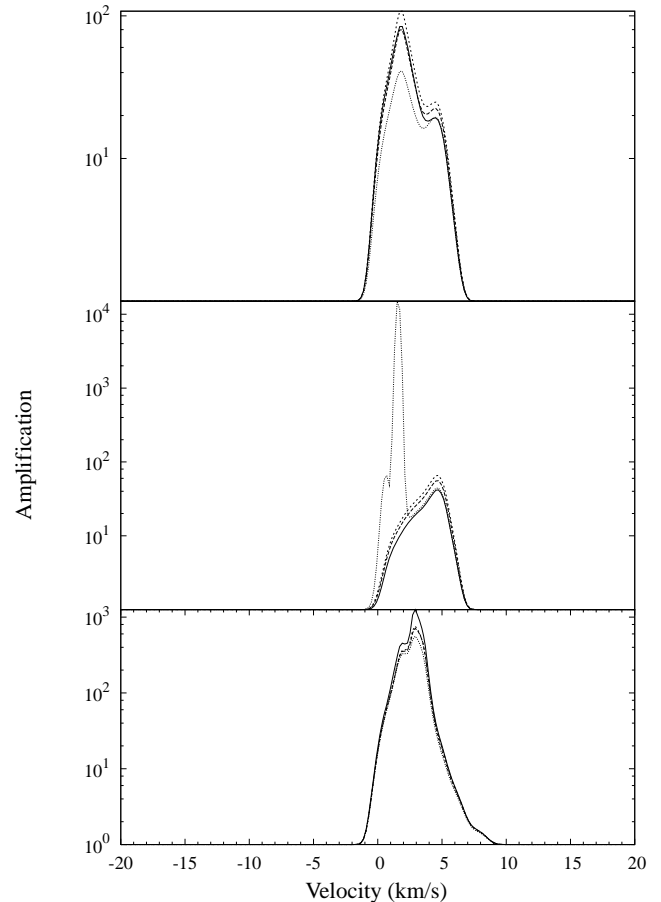
5.2 Variation of dust envelopes

We find that the effects of varying the dust epoch for the single hydrodynamic solution, M21n, vary from subtle shifts to profound change, depending on the transition in question. As an example, we show in Fig. 9, model spectra for three commonly observed lines. Beginning with the top panel, the 43 GHz $v = 1, J = 1$–0 line, we see that the spectra have very similar shapes for all four epochs, with a fairly subtle change in the amount of amplification introduced by varying the dust radiation field. In this line, Model 3, with dust epoch B, produces the brightest spectrum, with a peak amplification factor of 108, followed by Model 1 (epoch D dust) with 84, Model 2 (epoch C dust) with 80, and finally Model 4 (epoch A dust) with 41. Varying the dust radiation field therefore changes the peak maser amplification by a maximum factor of just over 2 in this line. The $v = 2, J = 1$–0 line (bottom panel in Fig. 9) also responds quite subtly to changes in the dust envelope, with very similar shapes for all four epochs. However, the brightness order is different from the analogous line in $v = 1$: here Model 1 yields the strongest line, though Model 4 is still the weakest.

In the 86 GHz line ($v = 1, J = 2$–1) we see a more profound, qualitative, effect of varying the parameters of the dust envelope. Spectra for this transition appear in the middle panel of Fig. 9.
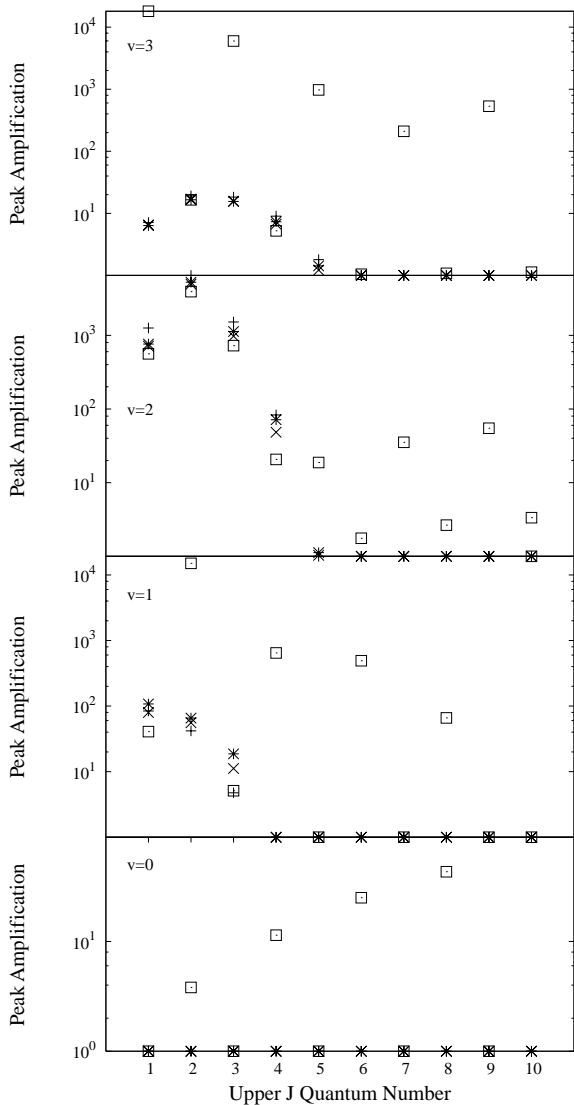
Figure 10. Peak amplification factors found in the spectra of the first ten rotational transitions (upper J quantum number on the x-axis) of the first four vibrational states of SiO (panels as marked with v increasing from bottom to top. Values for different dust epochs are marked with a different symbol: $+$ for Model 1 (epoch D), $\times$ for Model 2 (epoch C), $\ast$ for Model 3 (epoch B) and $\square$ for Model 4 (epoch A).

Model 4, with dust epoch A, which yields the weakest spectrum in both 43 GHz lines, introduces a strong additional peak on the blue side of the spectrum at 86 GHz, which is not present at the other three epochs.

A more general view of the effect of the dust radiation field on the SiO masers is presented in Fig. 10. Here we plot the peak amplification factor found in each spectrum. Each panel of the figure is a different vibrational state. Different symbols denote the dust epoch, and peak values are marked against upper J quantum number for transitions $J = 1$–0 up to $J = 10$–9. The main point to be drawn from Fig. 10 is that there is something special about Model 4, which uses dust epoch A, and is marked by the symbol $\square$. Model 4 is the only one of the four to generate any masers in $v = 0$, where inversions are only generated in transitions where the upper rotational level has even J. In the other vibrational states, only Model 4 has masers for upper $J > 5$; at lower J, the peak
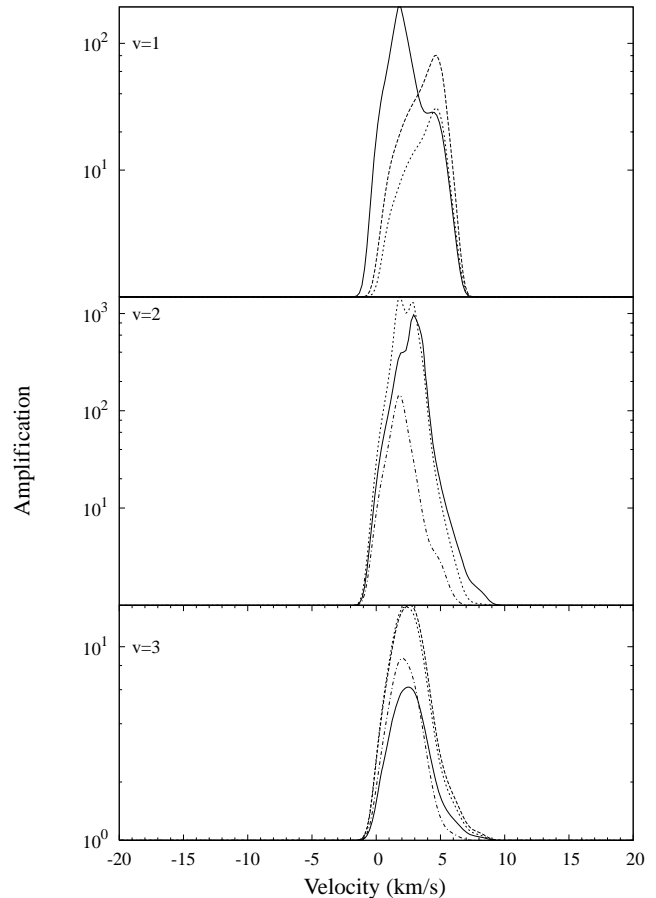

Figure 11. Spectra of the masers found in a dust-free model, based on the hydrodynamic solution M21n. Rotational transitions have the following line styles: $J = 1$–0 (solid), $J = 2$–1 (dashed), $J = 3$–2 (dotted), $J = 4$–3 (chained).

amplification values generated by the other three models are closely grouped, while the value for Model 4 is often very different. The middle panel of Fig. 9 is an example of this. The even-odd pattern produced by Model 4 in $v = 0$ is also echoed through the other v states: masers with upper J even are favoured in $v = 0$, 1, but masers with upper J odd are favoured in $v = 2$ and 3. We cannot, at present, explain the peculiarity of Model 4 in detail, but we note that in Fig. 5, the epoch A dust has the second-smallest inner dust shell radius, but a significantly higher dust temperature at its inner radius than the other three models.

If the inner ring of masers is considered, the effect of changing the dust parameters was much more marginal. The weaker, but 'standard' outer ring of spots is much more strongly affected individually, and when grouped into a spectrum, than those which were very intense.

To test the 'absolute' effect of dust, an additional model was run without a dust shell. In this model, pumping is entirely due to the radiation from the star (in Model M21n) and kinetic collisions. We show spectra for those lines in $v = 1$, 2 and 3 which showed significant maser emission in Fig. 11. As elsewhere, the $v = 2$, $J = 2$–1 line was excluded because of its interaction with a water transition.

When we compare the dust-free models to those with dust shells, we find that the largest effect is in $v = 1$, $J = 1$–0. The shape of the spectrum is similar, but if we compare the solid line in the top
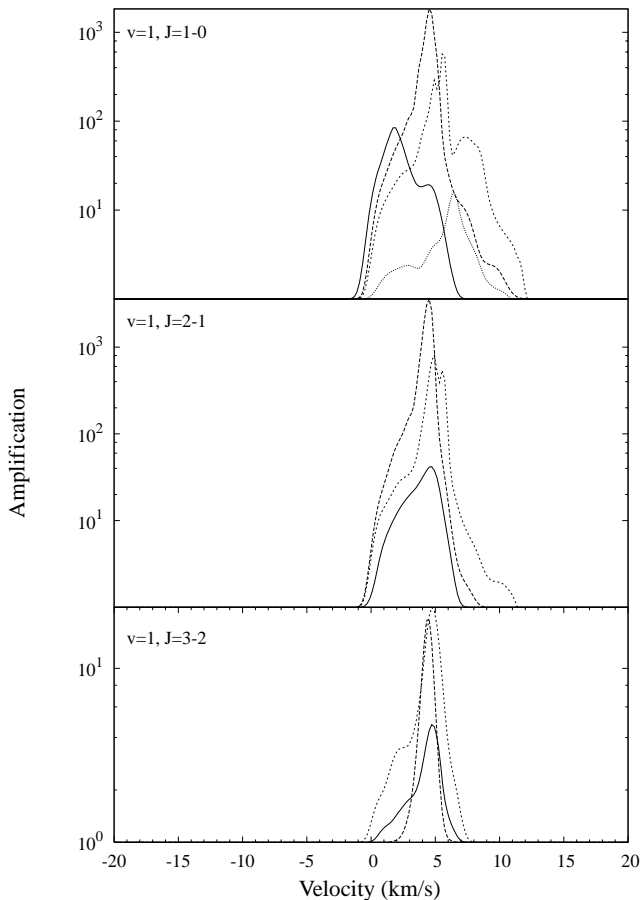
Figure 12. Spectra of the bright masers in $v = 1$ for the phase samples in Table 4. Each panel is for the transition as marked. Spectra in each panel have the following line styles: $\phi = 0.1$, Model 1 (solid line), $\phi = 0.25$, Model 5 (long-dashed line), $\phi = 0.30$, Model 6 (short-dashed line) and $\phi = 0.40$, Model 7 (dotted line).

Figure 13. As for Fig. 12, but for $v = 2$.

panel of Fig. 11 to the lines in the top panel of Fig. 9, we see that the peak in the dust-free case is brighter, by a factor of approximately 2, than the brightest case with a dust shell. For the other lines in Fig. 9 ($v = 2, J = 1$–0 and $v = 1, J = 2$–1) we again find similar shapes (with the exception of dust epoch A) and smaller changes in maser amplification. Overall then, the presence of Al_2O_3 dust can have both positive and (mildly) negative effects on maser pumping. We intend to investigate the effect of silicate dust, if present, in future work.

5.3 Phase samples

In the four phase samples listed in Table 4, no masers were found in $v = 0$. In $v = 3$, weak masers were found in rotational states up to $J = 5$–4, with the greatest amplification factor, of 19.2, at phase 0.1 (Model 1) in $v = 3, J = 2$–1. All the $v = 3$ masers followed a pattern of producing the strongest maser emission at phase 0.1, with a monotonic decay to phase 0.4. Only $J = 1$–0 and 2–1 masers survived to reach phase 0.4. In Fig. 12 we plot spectra of the three masers from $v = 1$ which achieve amplification factors of greater than 20. These form in the lowest three rotational transitions. Fig. 13 shows the spectra of bright masers from $v = 2$. Here, we ignore the $J = 2$–1 line because of its well-known interaction with a water
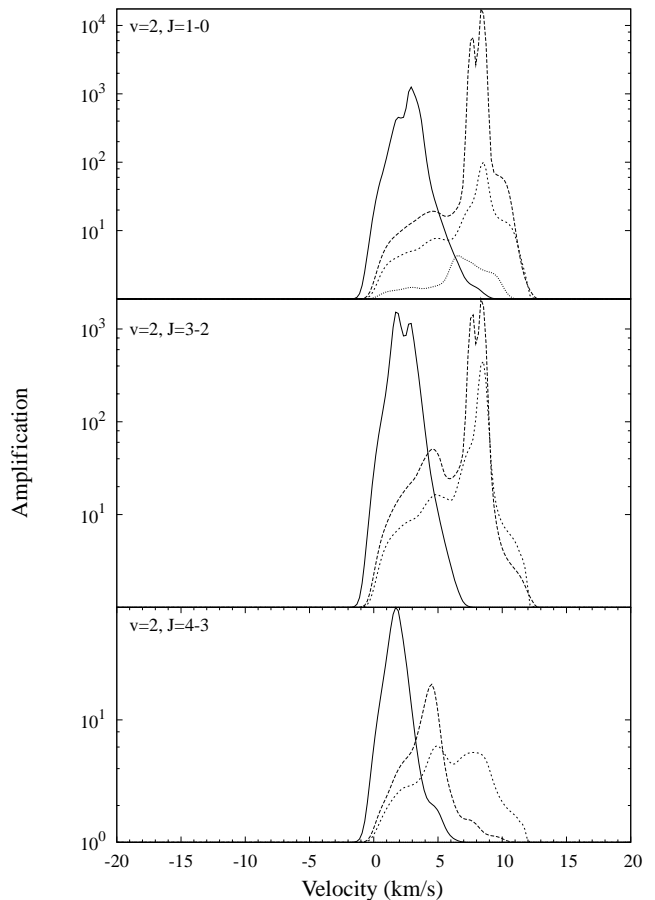
transition, so the plot consists of the masers in the $J = 1$–0, $J = 3$–2 and $J = 4$–3 transitions.

The main points to note from Fig. 12 are (i) the $J = 1$–0 line is the most stable: it is the only line which still emits as a maser at phase 0.4; (ii) the most favourable phase for masers is 0.25 (Model 8): both the $J = 1$–0 and $J = 2$–1 lines are strongest at this phase, and in $J = 3$–2 the maser from the next phase is only marginally stronger; (iii) in the $J = 1$–0 line, there appears to be a systematic redward shift of the spectral peak with phase, which does not seem to be the case in the other two lines.

In Fig. 13, we find that, as for $v = 1$, the $v = 2, J = 1$–0 line produces the most stable spectrum, with the only surviving emission at phase 0.4. The redward shift of the spectral peak with phase is apparent for all three lines shown in Fig. 13, with a very distinct shift between phases 0.1 and 0.25 in the $J = 1$–0 and $J = 3$–2 transitions. This shift significantly changes the shape of the spectra, while the peak moves to the red by $\sim 7 \, km \, s^{-1}$. The brightest phase is 0.25 for the $J = 1$–0 line, but 0.1 for the other two.

We now consider the spatial distribution of maser spots as a function of stellar phase in four transitions: $J = 1$–0 in $v = 1$ and $v = 2$, $v = 1, J = 2$–1 and $v = 2, J = 3$–2. The $v = 1, J = 1$–0 maser shell is shown in Fig. 14. The main change between phase 0.1 and the brightest phase (0.25) is a decrease in the ring radius, as judged by the brightest spots. After phase 0.25, there is a fading of the masers, with only a single obvious object remaining in the maps for phase 0.4. For the other 43 GHz line, $v = 2, J = 1$–0, we show its evolution with phase in Fig. 15. The behaviour is broadly similar to that of its counterpart in $v = 1$, but it is clearer that,
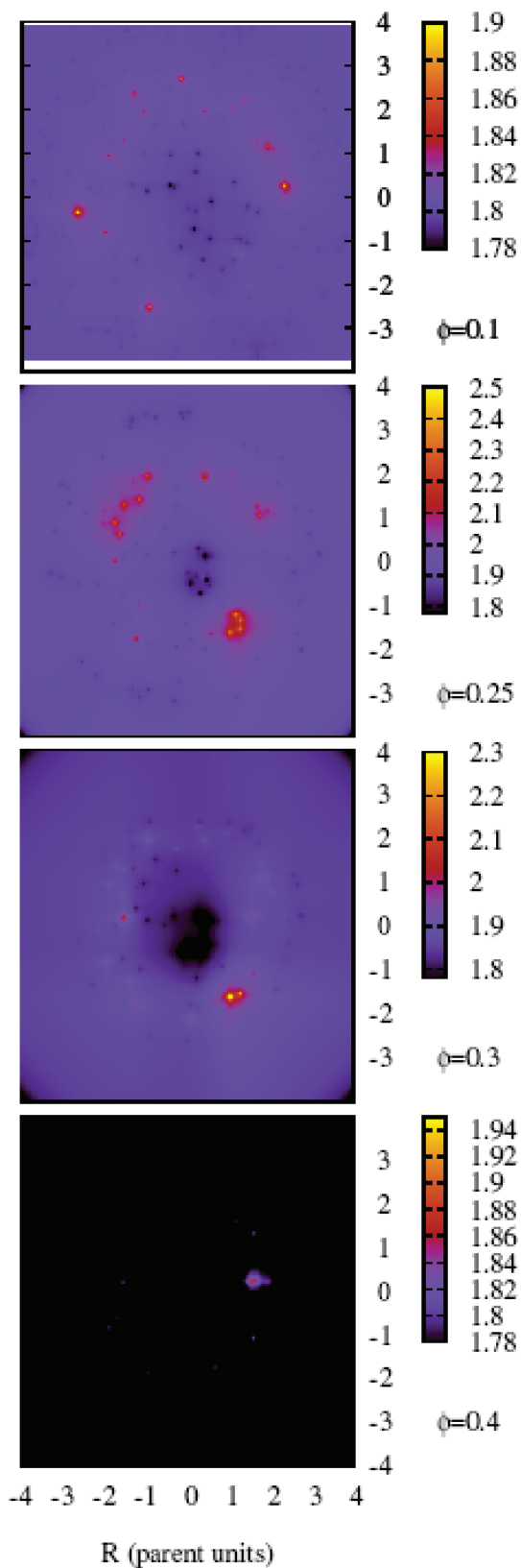
Figure 14. Maps of the spot distribution for masers in the $v = 1, J = 1\text{–}0$ transition for the four phase samples, as marked. The colour scale is in the logarithm to the base 10 of the amplification.
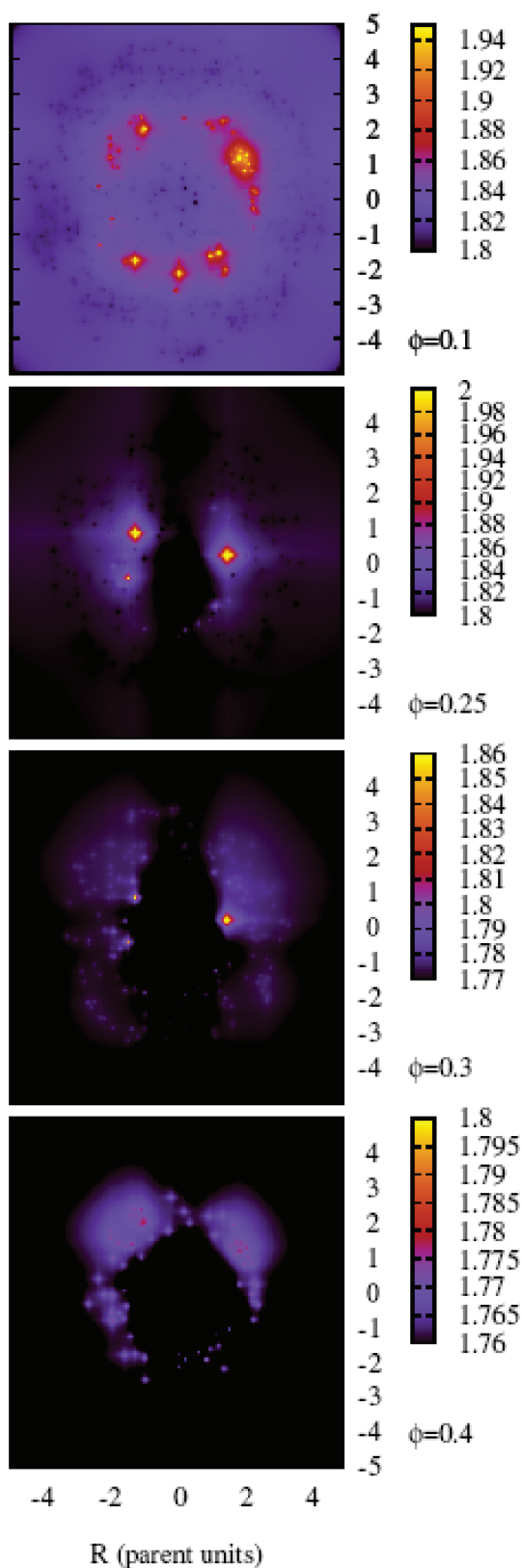
Figure 15. As Fig. 14, but for the $v = 2, J = 1\text{–}0$ transition.

Figure 16. As Fig. 14, but for the $v = 1, J = 2$–1 transition. No map is shown for phase 0.4 because the model produced no emission in this line for this phase.
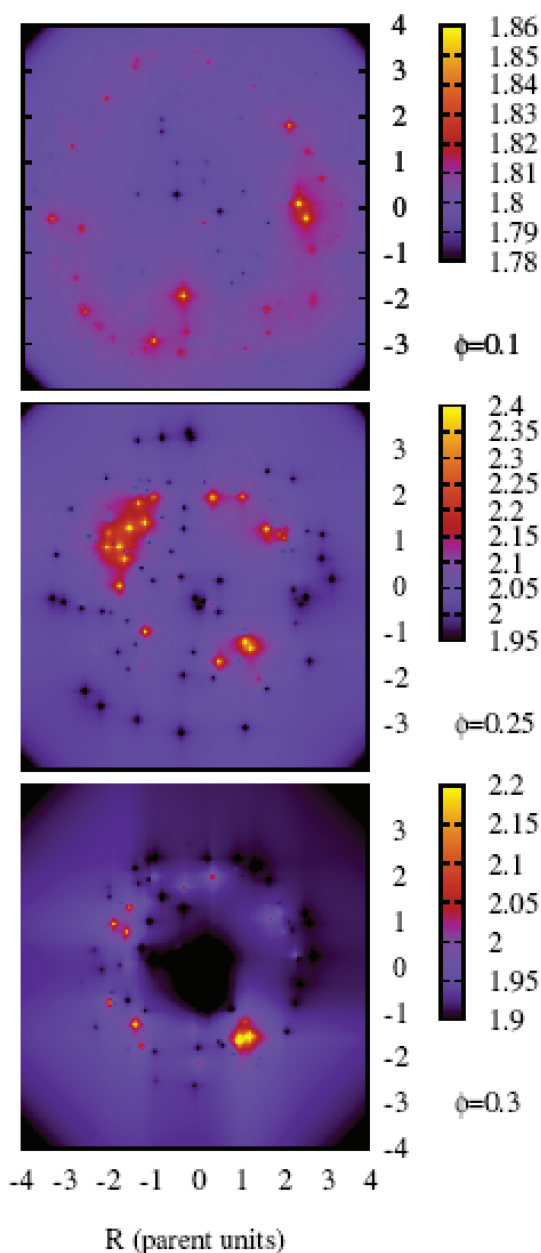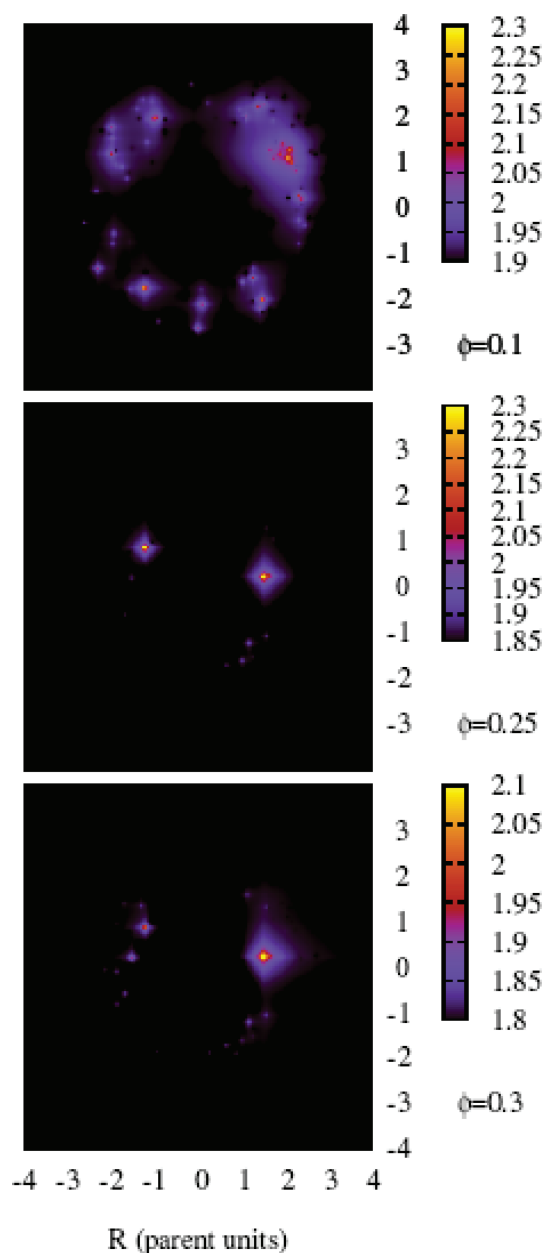
Figure 17. As Fig. 14, but for the $v = 2, J = 3$–2 transition. No map is shown for phase 0.4 because the model produced no emission in this line for this phase.

in the $v = 2$ transition, something catastrophic happens to the maser distribution between phases 0.1 and 0.25. Although the masers are brighter in the latter phase, the ring is smaller, indistinct and based on just a few very bright objects. These fade almost to extinction by phase 0.4. It is noticeable that in the map at phase 0.1, the region covered by weak maser emission is larger than for $v = 1$, so the $v = 2$ maps are plotted out to 5, rather than $4R_p$. The apparent north–south line of symmetry in the later phases in Fig. 15 results only from the random spot distribution and the mapping software, and does not result from any feature of the hydrodynamic solutions or dust shell. A comparison of Figs 14 and 15 phase by phase, suggests that, for the bright masers at least, the $v = 2$ spots occupy a smaller ring than those in $v = 1$. In Fig. 16, we show the maser shell of the 86-GHz transition, $v = 1, J = 2$–1. Only three phases

are shown, as there is no maser emission at phase 0.4. In this line, the ring structure is distinct through the three phases shown, but, as with the 43 GHz lines, there is evidence of a distinct change in structure, with a modestly strong, large radius maser ring ($\sim 3\,R_p$) replaced by an intense ring of radius $<2\,R_p$. The final set of maps we show, which is not yet observable with a VLBI interferometer, is the $v = 2, J = 3$–2 transition in Fig. 17. Like $v = 1, J = 2$–1, there is no emission at phase 0.4. The first two phases have very similar peak amplification, as seen in the spectrum in Fig. 13, but the spatial distribution of spots has still suffered a similar change in distribution to the other mapped transitions between phases 0.1 and 0.25. This change is also reflected in the spectrum of this line. The maser ring is arguably less rich than those from lower rotational states.

Extended structure visible in the all the maps in this paper (Figs 14–17 and 8) should be viewed with great caution. All the masers are actually point-like (see Section 3.3). The GNUPLOT software used to make the maps includes a gridding algorithm which smoothes the spot distribution into pixel values on a regular grid. The colour palette is then applied to these pixel values. However, there are typically several hundred low amplification maser spots which, when gridded and smoothed by the mapping software, yield the extended structure. If our distribution of low amplification points generates an equivalent flux to weak extended emission in real stars, could they explain observed discrepancies between the integrated flux from VLBI images and the flux from autocorrelation spectra? If we simply divide our spots into two classes of bright and weak, and assume that the masers in both classes have the same sizes and beaming angles, then the ratio of fluxes produced by the bright and weak objects is $N_b I_b / (N_w I_w)$, where N is the number of objects, subscripted with b for bright, or w for weak, and similarly for brightness, or specific intensities, I. As an example, we take the map for phase 0.1 in Fig. 14, and set the dividing line at spots with amplification factors of 200. We then have six bright and 256 weak spots. To obtain similar fluxes from the weak and bright populations we then need an average weak spot to be no fainter than 1/43 of the brightness of an average bright spot. On this basis our distribution of weak spots might possibly provide the flux missing from VLBI images.

6 DISCUSSION

The radio photosphere plays a vital role in reconciling the new model with observations. By selecting a rather large value of this parameter, a radius similar to $2R_p$, a group of extremely bright masers in an inner ring of projected radius $\sim 1R_p$ is excluded, leaving the remaining masers in a ring which is consistent with both observations and the old model. It is also useful to look at what else is obscured by selecting the large radio photosphere. In particular, the strong inner shock with a velocity change of $>20\,\mathrm{km\,s^{-1}}$, which is shown in Fig. 1 at a radius of 2.9×10^{13} cm, would not be visible in the radio. Our radio photosphere at this phase (0.1) has a radius of $2.2\,R_p$, or 3.98×10^{13} cm, so we would only be able to see the outer, highly damped, shock in Fig. 1, and the maximum observable velocity range in the envelope at radio frequencies is only $\sim 7\,\mathrm{km\,s^{-1}}$. Velocities of this magnitude, but not the $20\,\mathrm{km\,s^{-1}}$ of the inner shock, are in agreement with observations (Reid & Menten 2007), which measure the maximum velocity from the proper motions of SiO masers, and link these spatially to the radio photosphere with VLA continuum measurements. The damping of the shocks in the hydrodynamic solutions used in this paper is therefore an important improvement over the old model, in which the shocks were less well damped, and propagated at higher speeds for a given radius in the envelope.

The effects of dust can be both constructive and detrimental to the maser pump. The most spectacular effect is that the dust in Model 4 (epoch A) has a qualitatively different effect on maser emission when compared to the other three dust epochs, used in conjunction with the same hydrodynamic solution (M21n). We investigate briefly the origin of this behaviour, for which the $v = 1, J = 2-1$ line is a good example (see Fig. 9). On close examination, a single bright model spot is responsible for much of the extra peak in the spectrum of this line. This spot is positioned at a radius (unprojected) of $3.59\,R_p$, which is rather large, but the ring radius for this line is also larger than average (see discussion below and Fig. 16). This radius places the bright spot well within the epoch A dust

shell, very close to the ninth shell radius. We compared the dust mean intensity at the spot radius for all four epochs, and all the SiO IR pumping bands, but there is nothing peculiar about epoch A in this respect. It is therefore not the direct pumping power of the dust that makes epoch A different. A feature of the epoch A shell which is different from the other three epochs, with regard to the selected spot position, is a combination of high dust temperature, density and considerable depth into the shell. Epoch D has a higher dust temperature (1070 K versus 930 K), but the spot lies only between the third and fourth radii. The spot lies deeper inside the dust (near the 11th radius) in epoch B, but this shell has lower density and temperature (715 K). The most likely explanation for the particular behaviour of masers with dust from epoch A is therefore an optical depth effect, with the dust modifying the stellar IR continuum in the pumping bands. We intend to investigate the effects of dust further in future work.

The phase information in this paper is rather limited, so we have not attempted to follow the evolution of maser rings through the stellar cycle in a consistent way. We note also that in the modelling of S Ori, which used the same hydrodynamic solutions and dust shells, the fits to the observed optical phases (Wittkowski et al. 2007), and see Table 2, have a sequence which does not match that of the phases drawn directly from the theory. In spite of this, and following the theory-based phases, we find that the maser peak for all lines is in the phase range 0.1–0.25. This is consistent with the maser peak lagging the optical light somewhat. Given the error of 0.1 in the absolute phases from the model, this phase lag is consistent with typical observed lags between SiO masers and the optical light curve.

A distinct feature of all the maps is a structural change between phases 0.1 and 0.25, where the maser ring shows a decrease in radius and, usually, an increase in spectral output. This change in the structure of the map is accompanied, in some lines, by a redward shift in the spectral peak. There is also a shift from a large number of maser spots of modest brightness, to a smaller number of objects, a few of which are very intense. This behaviour may have some underlying cause related to the envelope dynamics, but as spot positions have been rerandomized, and not evolved, between the two phases, we can only suggest that this is an interesting feature, worthy of further investigation, rather than a hard result.

The new model allows us to be considerably more precise than the old model in studying the spatial relationship of the maser rings to each other, and to other important structures in the model, such as shocks, dust shells and optically thick layers. We display this information in Table 5. The first six columns of this table display model parameters, which are independent of the maser model. The remaining six columns show maser ring radii for the four transitions mapped in Figs 14–17. Of these six columns, the first four are ring radii from the present model, whilst the final two are from observations of S Ori, matched to theoretical phases as in Wittkowski et al. (2007). All radii given in Table 5 are relative to the IR photosphere (at 1.04 μm) for the particular phase for easy comparison with Wittkowski et al. (2007), table 7 and fig. 12.

Without even considering any maser ring radii, we can see that the 8.13 μm band radius (Column 6) is closely related to the position of the innermost shock (Column 3). The radii are the same to $0.1R_{1.04}$ for three epochs, but markedly different for epoch D (phase 0.1). This finding strongly suggests that the whole way of thinking about shocks propagating vast distances from some almost-fixed stellar photosphere, which caused many problems for the old model is simply outdated. For a significant portion of the cycle at least, the 8.13 μm radius is tied to a shock, so that the delay between

Table 5. Key radii for maser shells, and their association with shocks and optically thick band radii. All radii are written in terms of the IR photospheric value, $R_{1.04}$, at the appropriate phase. Columns are as follows: 1 – the hydrodynamic solution and dust epoch (the same as the observing epoch in Wittkowski et al. 2007); 2 – the stellar phase from theory (optical scale); 3 – radius of the inner shock; 4 – radius of the outer shock (not apparent at phase 0.4); 5 – inner radius of the dust shell; 6 – optically thick band radius in the $\Delta v = 1$ SiO pumping band; 7–10 – maser ring radii (in sky projection) with sample standard deviations for the transitions marked from the present model; 11 and 12 – observed maser ring radii from Wittkowski et al. (2007) for transitions as marked. In Columns 3 and 4, we have listed the radii for the same shocks. At phase 0.4, the original outer shock has damped out, so we have left the entry for R_{s2} blank at this phase. A new shock has formed at phase 0.4, with a radius of $1.0\,R_{1.04}$, inside the original inner shock, listed as R_{s1}.

Model + dust	Model parameters					Maser ring radii (photospheric units)					
	ϕ	R_{s1}	R_{s2}	R_{in}	$R_{8.13}$	$R_{43.1}$	$R_{42.8}$	$R_{v=1,J=2-1}$	$R_{v=2,J=3-2}$	$R_{43.1}^{obs}$	$R_{42.8}^{obs}$
M21n + D	0.1	1.3	2.5	2.4	1.8	1.9 ± 0.4	1.9 ± 0.4	2.4 ± 0.7	2.0 ± 0.4	–	–
M22 + A	0.25	1.6	2.6	1.8	1.6	1.9 ± 0.3	1.8 ± 0.3	1.8 ± 0.5	1.8 ± 0.3	2.2 ± 0.3	2.1 ± 0.2
M23n + C	0.3	1.7	2.8	2.2	1.7	1.9 ± 0.2	1.8 ± 0.2	1.9 ± 0.2	1.9 ± 0.2	2.1 ± 0.3	1.9 ± 0.2
M24n + B	0.4	2.0	–	2.0	2.0	2.1 ± 0.5	2.4 ± 0.4	–	–	2.4 ± 0.3	2.3 ± 0.4

irradiation and shock impact would be 25 d, or less. Consequently, many arguments which eliminate some element of collisional pumping on the grounds of long shock propagation times, relative to a distant, detached, stellar photosphere, are not relevant to resolving the pumping debate. The physical changes in the maser shells between phases 0.1 and 0.25 may be caused by the shift from a state where the 8.13 μm radius and inner shock are detached, to one where they are closely coupled.

The outer shock appears to be well outside the maser zone, except at phase 0.1, where it may be associated with the large $v = 1, J = 2$–1 ring (see Column 9). At most phases, the inner shock, the 8.13 μm radius and the maser ring radii of all the lines are within $0.3\,R_{1.04}$ of each other. This association does not involve the inner shock at phase 0.1. The inner edge of the Al_2O_3 dust, R_{in} (Column 5) is less well associated with masers, inner shock and 8.13 μm radius. It is close to the maser ring radius at phase 0.25 and 0.4, but not at phases 0.1 and 0.3.

The maser rings themselves are closely associated for almost all transitions and phases. The exception is the large ring at phase 0.1 for the $v = 1, J = 2$–1 transition. The ring radius for this transition is not peculiar at the other phases. In the first three phases, the mean ring radius of the $v = 2, J = 1$–0 masers is the same, or slightly smaller than that for the analogous transition in $v = 1$. This trend is swapped for phase 0.4, but this phase has a large standard deviation, due to the small number of surviving spots, and a rather poorly defined ring. At this phase, close to optical minimum, the masers from both $J = 1$–0 (43-GHz) transitions have their largest mean ring radii in both observations and theory. The model is therefore consistent with previous models and with VLBI observations which show that the $v = 2, J = 1$–0 ring is usually slightly smaller. The large ring for the $v = 1, J = 2$–1 masers at phase 0.1 is not in agreement with the old model, but is more in line with VLBI observations (Soria-Ruiz et al. 2007). The modelled ring radii at 43 GHz are also smaller than their observational counterparts, for the three phases where observational data exist. However, the ring sizes are consistent, given the standard deviations attached to these ring radii.

Maser spectra in the 43 GHz ($J = 1$–0) lines have velocity extents of $\sim 10\,\mathrm{km\,s^{-1}}$, a value which is consistent with the observational spectra of these lines towards S Ori (Wittkowski et al. 2007). The LSR velocity of S Ori is not very well known, so we have not computed Doppler biases for our spectra, though these model spectra are certainly concentrated to the red side of the velocity range.

Perhaps the largest drawback of this paper, in terms of matching VLBA observations of S Ori, is in the variation of spectral intensity. In the three observed phases, the ratio of the spectral maxima for the brightest and dimmest phases is about 1.5 for the $v = 1, J =$ 1–0 line, and about 2 for $v = 2, J = 1$–0. By contrast, the fading of the model masers towards phase 0.4 gives analogous ratios of approximately 70 and 1000. However, as has been noted previously, our models are not evolved in phase, but use repositioned spots, so the numbers could be very different if the masers followed the gas motions. There are also only a small number of bright spots, so these ratios are very vulnerable to statistical fluctuations.

7 CONCLUSIONS

The new combined maser and hydrodynamic solutions produce maser emission in rings of typical size 2.2 IR photospheric radii. The ring structures are similar in many respects to those produced by the old model. An analysis of ring radii confirms the usual observational result, and the prediction of the old model, that the $v = 2$ ring is smaller than the $v = 1$ ring at 43 GHz, whilst a large ring is possible at some phases in the $v = 1, J = 2$–1 transition at 86 GHz. The overall range of maser ring radii, from 1.8 to 2.4 IR photospheric radii, for the 43-GHz transitions in $v = 1$ and 2 is also consistent with VLBI experiments where maser rings and photospheric radii have been compared at the same phase (Boboltz & Wittkowski 2005; Fedele et al. 2005; Wittkowski et al. 2007).

If a radio photosphere of approximately 2 IR photospheric radii is used, observable shock velocities are in agreement with actual radio continuum observations, as high-velocity shocks, such as the inner shock at phase 0.1, are hidden. A radio photosphere of this size also prevents the appearance of extremely bright masers very close to the IR photosphere.

Dust can both suppress and enhance maser emission, and there is definitely a radiative component to the pumping scheme. However, the close association of shock and 8.13 μm radii suggests that collisional and radiative pumping are closely associated spatially, and therefore temporally.

Further work is required to consider the effects of dust in detail, and to produce a fully phase-sampled model of one or more complete stellar cycles.

REFERENCES

Begemann B., Dorschner J., Henning Th., Mutschke H., Guertler J., Koemper C., Nass R., 1997, ApJ, 476, 199

Bieniek R., 2008, A&AS, 212, 3.26

Boboltz D. A., Wittkowski M., 2005, ApJ, 618, 953

Boboltz D. A., Diamond P. J., Kemball A. J., 1997, ApJ, 487, L147

Bowen G. H., 1988, ApJ, 329, 299

Bowen G. H., 1990, Ann. New York Acad. Sci., 617, 104

Cherchneff I., 2006, A&A, 456, 1001

Cotton W. D. et al., 2004, A&A, 414, 275

Cotton W. D. et al., 2006, A&A, 456, 339

Decin L., Cherchneff I., Hony S., Dehaes S., De Breuck C., Menten K. M., 2008, A&A, 480, 431

Desmurs J.-F., Bujarrabal V., Colomer F., Alcolea J., 1999, New Astron. Rev., 43, 559

Desmurs J.-F., Bujarrabal V., Colomer F., Alcolea J., 2000, A&A, 360, 189

Diamond P. J., Kemball A. J., 2003, ApJ, 599, 1372

Diamond P. J., Kemball A. J., Junor W., Zensus A., Benson J., Dhawan V., 1994, ApJ, 430, L61

Fedele D., Wittkowski M., Paresce F., Scholz M., Wood P. R., Ciroi S., 2005, A&A, 431, 1019

Gray M. D., Humphreys E. M. L., 2000, New Astron., 5, 155

Gray M. D., Humphreys E. M. L., Field D., 1995a, Ap&SS, 224, 63

Gray M. D., Ivison R. J., Yates J. A., Humphreys E. M. L., Hall P. J., Field D., 1995b, MNRAS, 277, L67

Gray M. D., Ivison R. J., Humphreys E. M. L., Yates J. A., 1998, MNRAS, 295, 970

Gray M. D., Humphreys E. M. L., Yates J. A., 1999, MNRAS, 304, 906

Greenhill L. J., Colomer F., Moran J. M., Backer D. C., Danchi W. C., Bester M., 1995, ApJ, 449, 365

Hofmann K.-H., Scholz M., Wood P. R., 1998, A&A, 339, 846

Humphreys E. M. L., Gray M. D., Yates J. A., Field D., Bowen G., Diamond P. J., 1996, MNRAS, 282, 1359

Humphreys E. M. L., Gray M. D., Field D., Yates J. A., Bowen G., 1997a, Ap&SS, 251, 215

Humphreys E. M. L., Gray M. D., Field D., Yates J. A., Bowen G., 1997b, MNRAS, 287, 663

Humphreys E. M. L., Gray M. D., Yates J. A., Field D., Bowen G., Diamond P. J., 2002, A&A, 386, 256

Ireland M. J., Scholz M., 2006, MNRAS, 367, 1585

Ireland M. J., Scholz M., Wood P. R., 2004a, MNRAS, 352, 318

Ireland M. J., Scholz M., Tuthill P. G., Wood P. R., 2004b, MNRAS, 355, 444

Ireland M. J., Scholz M., Wood P. R., 2008, MNRAS, 391, 1994

Jimeno P., Gray M. D., Balint-Kurti G. G., 1999, J. Chem. Phys., 111, 4966

Koike C., Kaito C., Yamamoto T., Shibai H., Kimura S., Suto H., 1995, Icarus, 114, 203

McIntosh G. C., 2006a, ApJ, 638, 41

McIntosh G. C., 2006b, ApJ, 649, 406

McIntosh G. C., Haynes A. M., 2007, ApJ, 678, 1324

Nakashima J., Deguchi S., 2007, ApJ, 669, 446

Ohnaka K., 2004, A&A, 424, 1011

Ohnaka K. et al., 2006a, A&A, 445, 1015

Ohnaka K., Scholz M., Wood P. R., 2006b, A&A, 446, 1119

Ossenkopf V., Henning Th., Mathis J. S., 1992, A&A, 261, 567

Palov A., Jimeno P., Gray M. D., Field D., Balint-Kurti G. G., 2002, 116, 1388

Palov A., Gray M. D., Field D., Balint-Kurti G. G., 2006, ApJ, 639, 204

Pardo J. R., Alcolea J., Bujarrabal V., Colomer F., del Romero A., de Vicente P., 2004, A&A, 424, 145

Perrin G. et al., 2004, A&A, 426, 279

Ragland S. et al., 2008, ApJ, 679, 746

Reid M. J., Menten K. M., 1997, ApJ, 476, 327

Reid M. J., Menten K. M., 2007, ApJ, 671, 2068

Scholz M., 2003, in Traub W. A., ed., SPIE Conf. Ser. Vol. 4838, Interferometry for Optical Astronomy II. SPIE, Bellingham, p. 163

Scholz M., Takeda Y., 1987, A&A, 186, 200

Soria-Ruiz R., Alcolea J., Colomer F., Bujarrabal V., Desmurs J.-F., Marvel K. B., Diamond P. J., 2004, A&A, 426, 131

Soria-Ruiz R., Alcolea J., Colomer F., Bujarrabal V., Desmurs J.-F., 2007, A&A, 468, L1

Tej A., Lançon A., Scholz M., Wood P. R., 2003, 412, 481

Thompson R. R., Creech-Eakman M. J., van Belle G. T., 2002, ApJ, 577, 447

Weigelt G., Balega Y., Hofmann K.-H., Scholz M., 1996, A&A, 316, L21

Willson L. A., 1987, in Kwok S., Pottasch S. R., eds, Late Stages of Stellar Evolution. Dordrecht, Reidel, p. 253

Willson L. A., 2000, ARA&A, 38, 573

Wittkowski M., Boboltz D. A., Ohnaka K., Driebe T., Scholz M., 2007, A&A, 470, 191

Wittkowski M., Boboltz D. A., Driebe T., Le Bouquin J.-B., Millour F., Ohnaka K., Scholz M., 2008, A&A, 479, L21

Woodruff H. C., Tuthill P. G., Monnier J. D., Ireland M. J., Bedding T. R., Lacour S., Danchi W. C., Scholz M., 2008, ApJ, 673, 418

Yi J., Booth R. S., Conway J., Diamond P. J., Winnberg A., 2000, in Conway J. E., Polatidis A. G., Booth R. S., Pihlström Y., eds, Proc. 5th EVN Symp. Onsala Space Observatory, Sweden, p. 193

Yi J., Booth R. S., Conway J., Diamond P. J., 2005, A&A, 432, 531

This paper has been typeset from a T$_{\rm E}$X/L$^{\rm A}$T$_{\rm E}$X file prepared by the author.